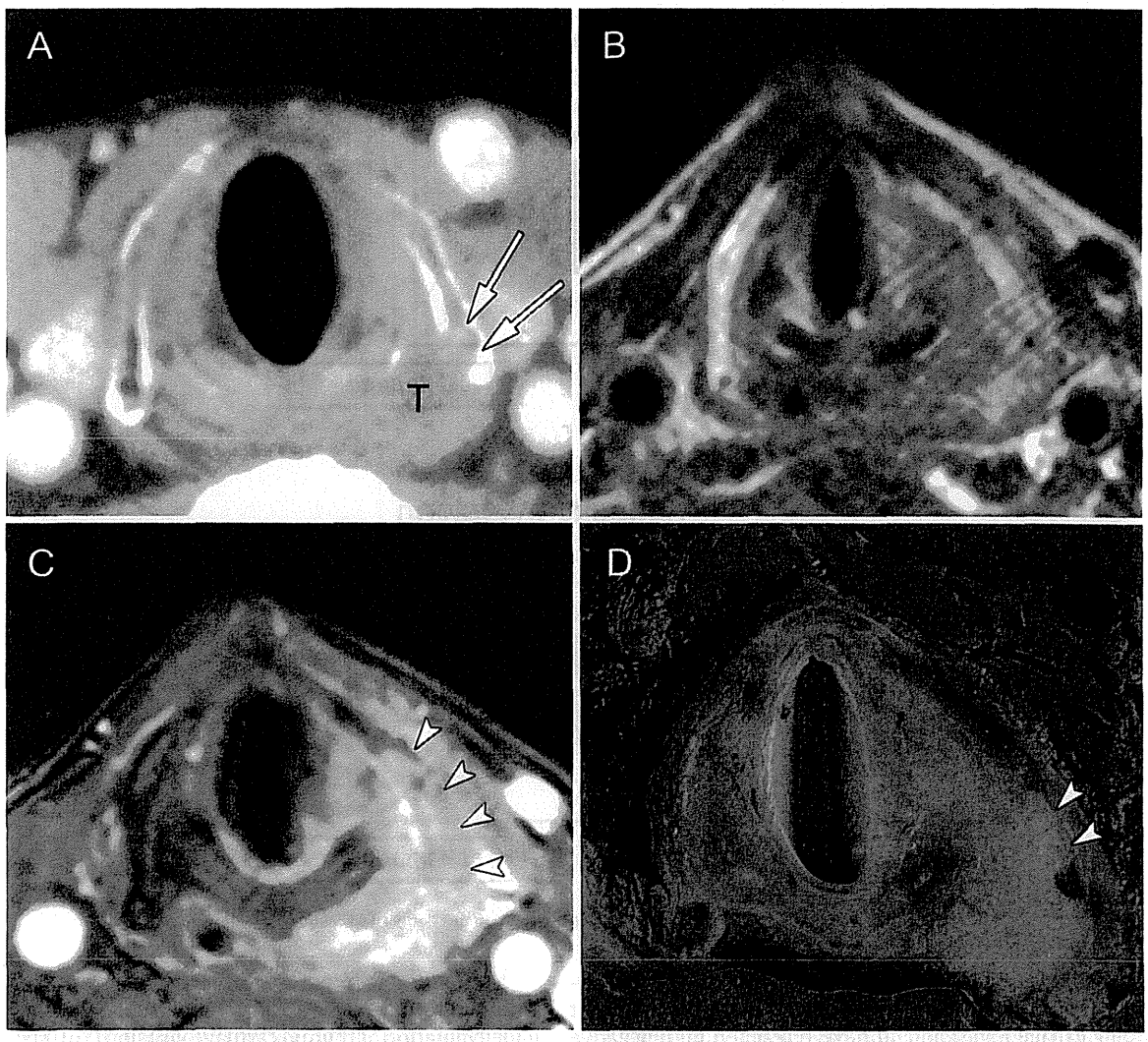

Fig. 7. Hypopharyngeal cancer in a 67-year-old man with thyroid cartilage invasion. (A) Axial contrast-enhanced CT image at the subglottic level shows a tumor mass (T) arising from the right piriform sinus with evidence of focal lysis on the left thyroid cartilage (arrows). (B) T2-weighted MR image obtained at the same level shows a left-sided piriform sinus tumor with intermediate signal intensity. As the motion artifacts are strong, no anatomical information can be obtained in that area and tumor invasion cannot be identified. (C) Fat-suppressed contrast-enhanced T1-weighted image shows more extensive contrast enhancement of the tumor mass and thyroid cartilage than the CT findings. (D) A corresponding slice of the surgical specimen shows the focal infiltration of the tumor into cartilage (arrowheads), consistent with the findings of CT imaging. Thus, the range of tumor cell invasion was overestimated on the fat-suppressed contrast-enhanced T1-weighted MR image.

with cartilage invasion, CT may easily identify tumor growth outside the larynx with cartilage invasion to the soft tissues of the neck (Fig. 2C). This finding is the most reliable criterion of invasion, but is evident only in advanced cases. When determining whether erosion or lysis is present or absent, differentiation from cartilage invasion may sometimes be difficult using conventional CT (Fig. 2B). Some cases may be distinguished from erosion if two concurrent findings of negativity are identified (Fig. 3A): a perfect or almost continuously defined thin hypo-attenuating line between the tumor and the cartilage (Fig. 3B), and CT attenuation of non-ossifying cartilage that differs from that of the tumor (Fig. 3C). However, distortion of adjacent normal structures may mimic tumor involvement, even with careful evaluation.

Asymmetrical sclerosis, defined as thickening of the cortical margin, increased medullary density, or both, when comparing one arytenoid with the other, or one side of the cricoid or thyroid cartilage with the other side, is a sensitive but non-specific feature of cartilage invasion on CT [26,40–42]. For the thyroid cartilage, asymmetric sclerotic changes (ossification) without erosion or lysis should not be diagnosed as positive, as these changes sometimes represent reactive inflammatory changes [26].

The introduction of multi-slice CT has resulted in an increase of spatial and temporal resolution but has led to little progress in interpretation of cartilage invasion [43], which is still sometimes overestimated [9,10]. A fundamental problem of CT is that laryngeal non-ossified cartilage and tumors show similar CT values of about 100 HU, making them almost indistinguishable, especially when the tumor is located adjacent to non-ossified cartilage (Fig. 4A) [8,26]. In addition, the appearance of laryngeal cartilage on CT varies widely according to differences in the proportions of hyaline cartilage (which ossifies with aging), cortical bone, and fatty marrow, which complicates interpretation.

4.1.2. MR imaging

MR imaging seems to be more sensitive than CT for detecting thyroid cartilage invasion (sensitivity up to 96%), as the high contrast resolution of MR makes it possible to detect small areas of marrow space invasion [18,38,44,45]. When assessing cartilage invasion with MR imaging, the T2-weighted and contrast-enhanced T1-weighted signal intensities of the cartilage should be compared with the signal intensities of the adjacent tumor [45]. If the cartilage displays a signal intensity similar to that of the tumor, cartilage

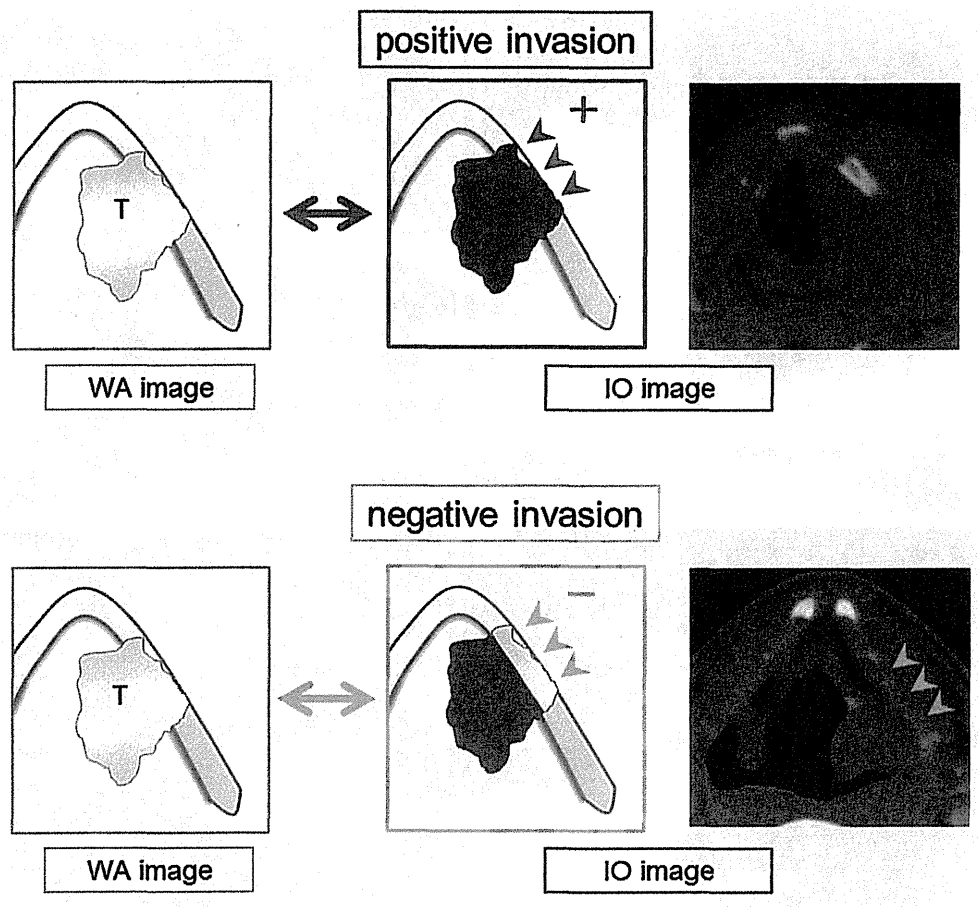

Fig. 8. Criteria for evaluation of cartilage invasion on dual-energy CT WA and IO images.

invasion should be suspected (Fig. 5). Contrast-enhanced MR imaging is also useful when evaluations by CT alone are insufficient for excluding cartilage invasion, and have reached high negative predictive values of up to 96% (Fig. 4) [38,45].

However, the MR findings suggestive of cartilage invasion are not specific, and therefore may lead to a number of false positive signs. The reason is that reactive inflammation, edema and fibrosis in the vicinity of a tumor may demonstrate diagnostic features similar to those of cartilage invasion (Fig. 6). Inflammatory changes are most common in the thyroid cartilage, and therefore the specificity of MR imaging for detecting invasion of the thyroid cartilage is only 56–65% [38,45]. Furthermore, MR resolution is often degraded by motion artifacts [45] and lacks thin sections (Fig. 7B), and the area of tumor extension into cartilage is more easily overestimated on MR imaging than on CT (Fig. 7C). Both of these factors mean that MR imaging is not a satisfactory first choice for imaging of laryngeal and hypopharyngeal cancer.

4.1.3. Dual-energy CT

The recommended dual-energy CT criteria for laryngeal cartilage invasion are summarized in Fig. 8. The IO images are read in addition to the WA images to identify the iodine distribution corresponding to the area displayed on the WA images. After a lesion has been evaluated as positive on WA images, the iodine distribution on the IO images is examined to derive a final classification of either positive or negative. When the IO image shows a corresponding area of tumor cartilage invasion as a red-colored area, positive invasion can be considered based on the combined findings evident on WA and IO images (Fig. 9). When the IO image does not show a corresponding area of tumor cartilage invasion as a red-colored area, tumor invasion can be defined as negative (Fig. 10).

A preliminary report suggests that dual-energy CT has the potential to increase diagnostic performance and reproducibility for evaluation of thyroid cartilage invasion [16]. The reported specificity of combined analysis of WA and IO images obtained with dual-energy CT is significantly superior to that of WA imaging alone (96% vs. 70%) with no compromise of sensitivity (86% vs. 86%), and the interobserver reproducibility of diagnosis using a combination of WA plus IO images is higher than that with WA imaging alone (especially for evaluation of thyroid and cricoid cartilage invasion) [16], and also that reported in a few studies using single-section spiral CT [46,47].

When interpreting the findings of dual-energy CT, it is important to be aware of certain technical limitations. Since this technique applies a 3-material decomposition algorithm with soft tissues and iodine as predefined materials [12,13,33], bone and calcified structures are classified into iodine or soft tissues according to tissue density, and cannot be clearly identified on IO images. As a result, lesions that include calcified structures such as sclerosis and previously ossified parts of cartilage need to be evaluated on WA images first, because on IO images iodine distribution may be overestimated. This does not create an advantage or disadvantage compared to conventional CT, since WA images already have image quality similar to that of conventional CT images. In short, diagnostic reading should always start with the WA image, followed by additional reading of the IO image when appropriate [16].

4.2. Extralaryngeal tumor spread

Extralaryngeal tumor spread is considered to be present when the primary tumor has expanded into extralaryngeal soft tissues, such as cervical soft tissues, the infrahyoid muscles, thyroid gland,

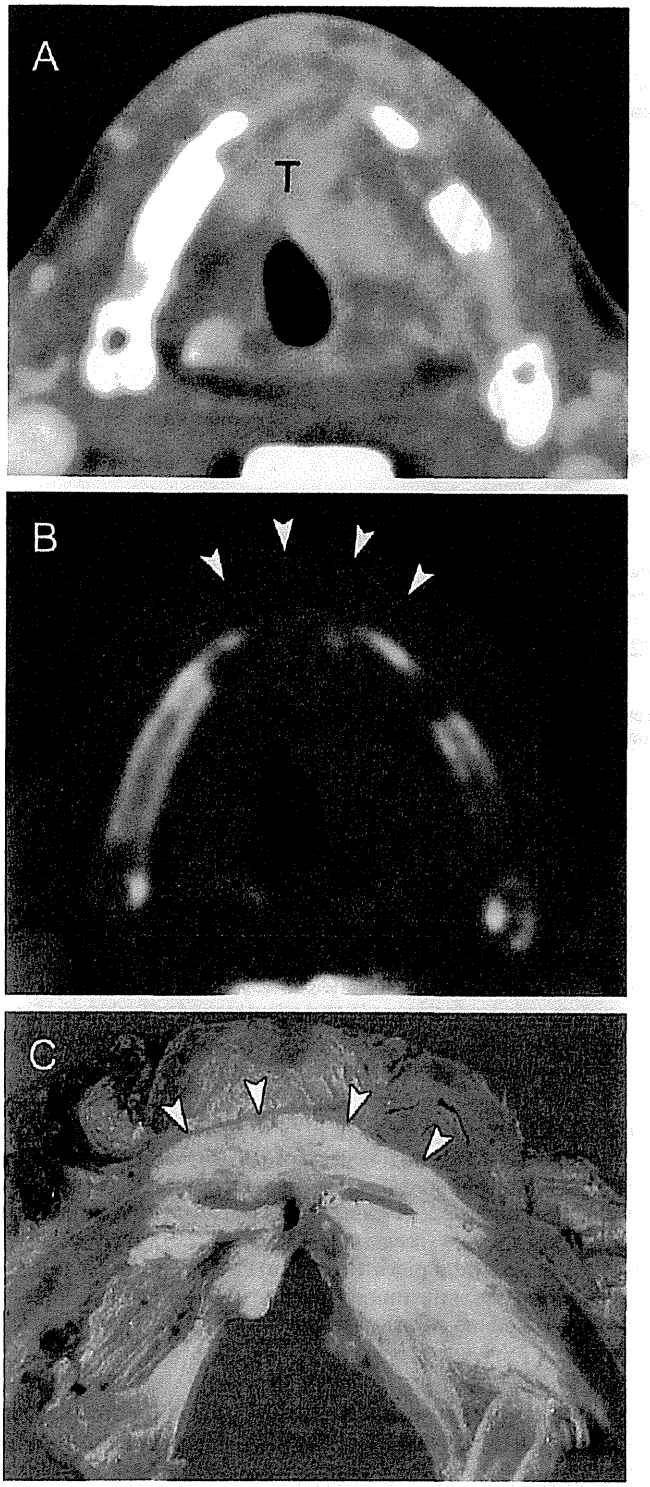

Fig. 9. Positive finding of thyroid cartilage invasion through the outer cortex by dual-energy CT in a 60-year-old man with supraglottic cancer. (A) WA image at the glottic level shows tumor (T) invasion into the thyroid cartilage, spreading into the extralaryngeal soft tissue. (B) On the IO image, the extent of extralaryngeal tumor spread is clearly evident (arrowheads). (C) A corresponding slice of the surgical specimen shows the tumor cell penetrates through the cartilage and invades the extralaryngeal soft tissue (arrowheads), consistent with the findings of the IO image.

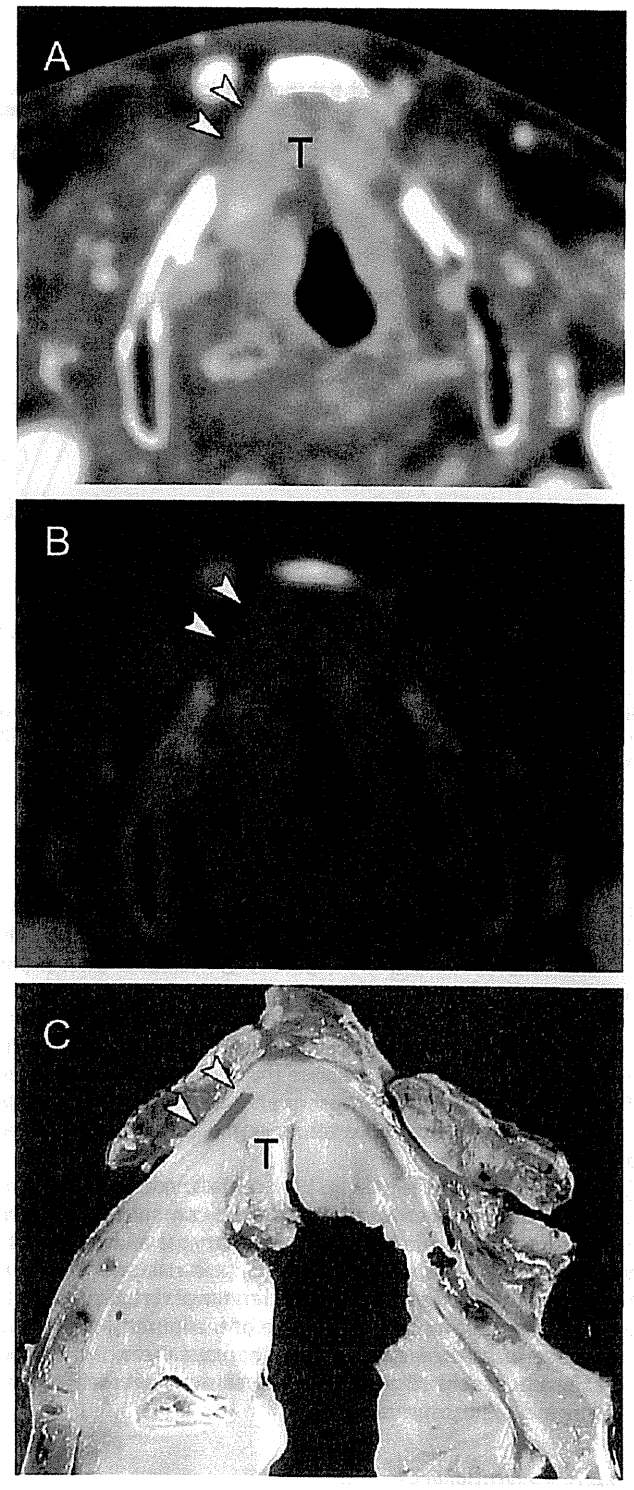

Fig. 10. Negative finding for erosion in the thyroid cartilage by dual-energy CT in a 68-year-old man with glottic cancer. (A) WA image at the level of the vocal cords shows a tumor mass (T) that has invaded the paraglottic space. Non-ossified cartilage of the right thyroid lamina has been substituted by the tumor (arrowheads). (B) IO image clearly shows no corresponding enhancement of the thyroid cartilage (arrowheads). (C) The corresponding slice of the surgical specimen shows that the right thyroid cartilage has not been invaded by the tumor cells (arrowheads).

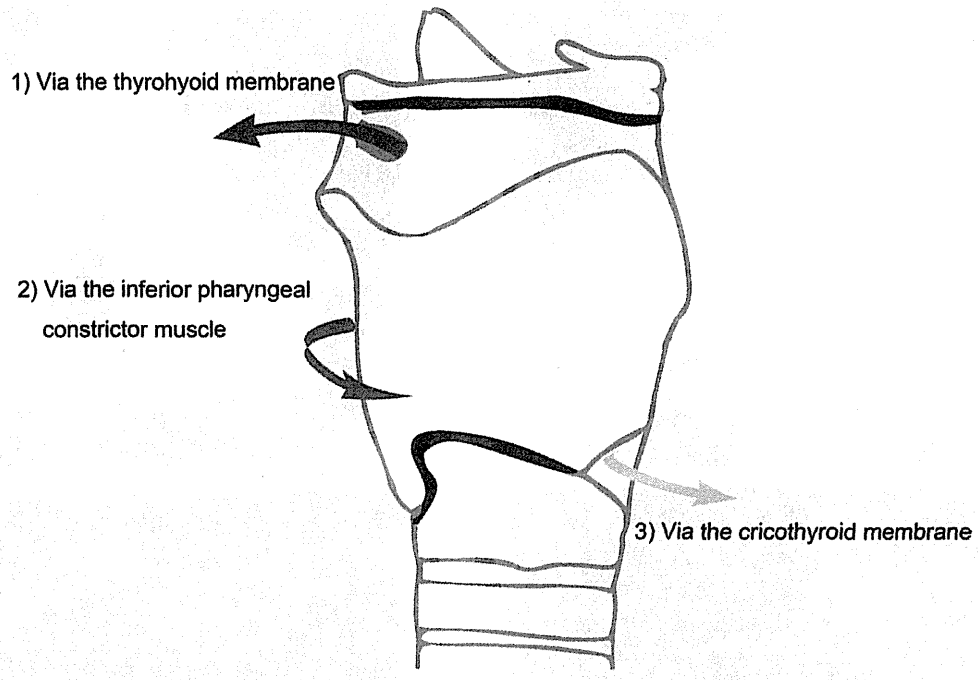

Fig. 11. Drawings (right lateral view of laryngeal box) illustrate the routes of tumor spread out from the larynx through areas of inherent weakness; (1) via the thyrohyoid membrane along the superior laryngeal neurovascular bundle (red arrow), (2) via the inferior pharyngeal constrictor muscle (blue arrow), (3) via the cricothyroid membrane (yellow arrow).

esophagus, trachea, or deep lingual muscle, with or without cartilage penetration [20]. In clinical practice, patients with T4 disease do not always inevitably undergo laryngectomy, and for patients without tumor extension through the cartilage – a diagnosis that is not always straightforward – clinicians rely on imaging for accurate tumor staging, tumor mapping and detection of possible tumor extension [5,6]. It is then possible to predict which patients may be candidates for function-preserving treatments to some degree, and discussions with the patients are part of the treatment decision process.

According to Beitler et al. [39], extralaryngeal spread without thyroid cartilage penetration was more common than previously expected in patients with advanced laryngeal and hypopharyngeal cancer. The authors suggested that cartilage invasion was absent in 40% of cases showing extralaryngeal tumor spread. Since extralaryngeal tumor spread is one of the important predictors of T4 disease in laryngeal and hypopharyngeal cancer, the focus of imaging needs to shift from detection of invasion to reliably demonstrating more extensive disease.

4.2.1. Conventional CT

Extralaryngeal spread can be considered if the following features can be identified: substitution by tumor tissue on the outside of the membrane/cartilage, or loss of fat attenuation between the extralaryngeal structure (such as blood vessel or muscle) and laryngeal components. To detect extralaryngeal spread, it is important to thoroughly understand the complex anatomy in this area and the imaging features of commonly occurring extension patterns (Fig. 11). One of the most common routes of lesion spread from the larynx through areas of inherent weakness is via the thyrohyoid membrane (Fig. 12). The superior laryngeal neurovascular bundle enters the laryngeal component through a posterolateral defect in the thyrohyoid membrane; this defect is known to be the route by which tumors spread [48,49]. Another route of extralaryngeal spread, especially in the case of piriform sinus cancer, is via the inferior pharyngeal constrictor muscle [48,50] on the basis of its attachment to the lamina of the thyroid cartilage (Fig. 13). Sometimes, the tumor may show submucosal extension to the extralaryngeal soft tissue via the cricothyroid membrane (Fig. 14). Such extension into deep-seated tissue planes is difficult to evaluate by clinical inspection examination alone.

4.2.2. MR imaging

Diagnosis of extralaryngeal spread on the basis of MR imaging is based mainly on altered signal behavior of extralaryngeal soft tissue with different pulse sequences. Extralaryngeal spread is considered to be present when signals in the fat component of extralaryngeal soft tissue continuous with the primary tumor have an intensity similar to that of the tumor on T2WI, are hypointense on T1WI, and hyperintense on contrast-enhanced T1WI.

4.2.3. Dual-energy CT

Extralaryngeal spread can be identified on CT or MR imaging, but dual-energy CT may facilitate a clearer diagnosis. The IO images generated by using dual-energy CT reveal the area of tumor spread into soft tissue as red-colored enhancement, because IO images visualize areas of iodine distribution in soft tissue (Figs. 12B, 13B and 14C). The preliminarily reported sensitivity and specificity of WA plus IO images for extralaryngeal spread are 100% (14/14) and 100% (16/16), respectively [16]. Regardless of whether cartilage invasion is present, combined analysis of WA and IO images may also be useful for evaluating extralaryngeal spread of advanced laryngeal and hypopharyngeal cancer.

5. A diagnostic algorithm including dual-energy CT

All patients with symptoms that are suggestive of laryngeal or hypopharyngeal cancer should undergo a thorough assessment

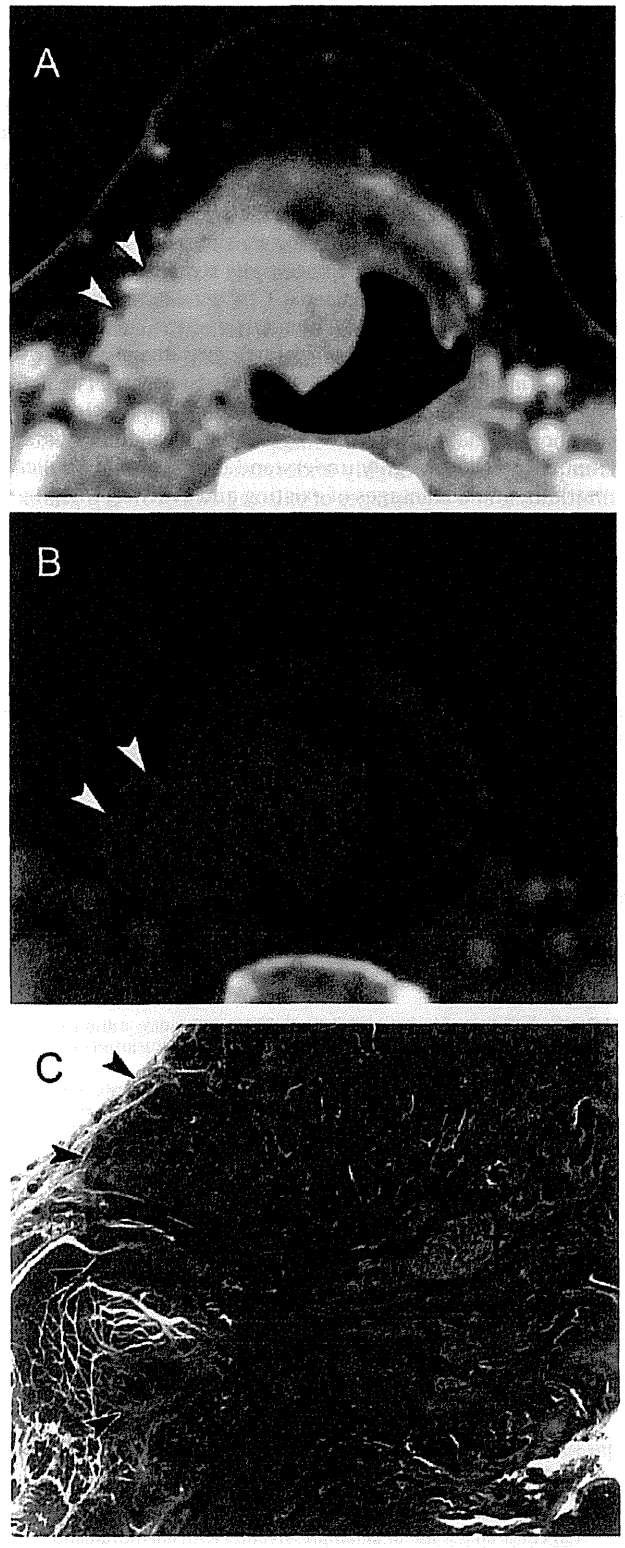

Fig. 12. Extralaryngeal spread via the thyrohyoid membrane on dual-energy CT in a 78-year-old man with supraglottic cancer. (A) WA image shows that the tumor has invaded the right aryepiglottic fold and preepiglottic space at the superior margin of the thyroid cartilage. The tumor extends through the thyrohyoid membrane into the extralaryngeal tissues (arrowheads). (B) The IO image reveals extralaryngeal tumor spread more clearly through the thyrohyoid membrane along the superior neurovascular bundle as a red-colored area (arrowheads). (C) Microscopic analysis confirmed the infiltration of the tumor cells into the extralaryngeal soft tissue and thyrohyoid muscle (hematoxylin–eosin stain; original magnification, 5×).

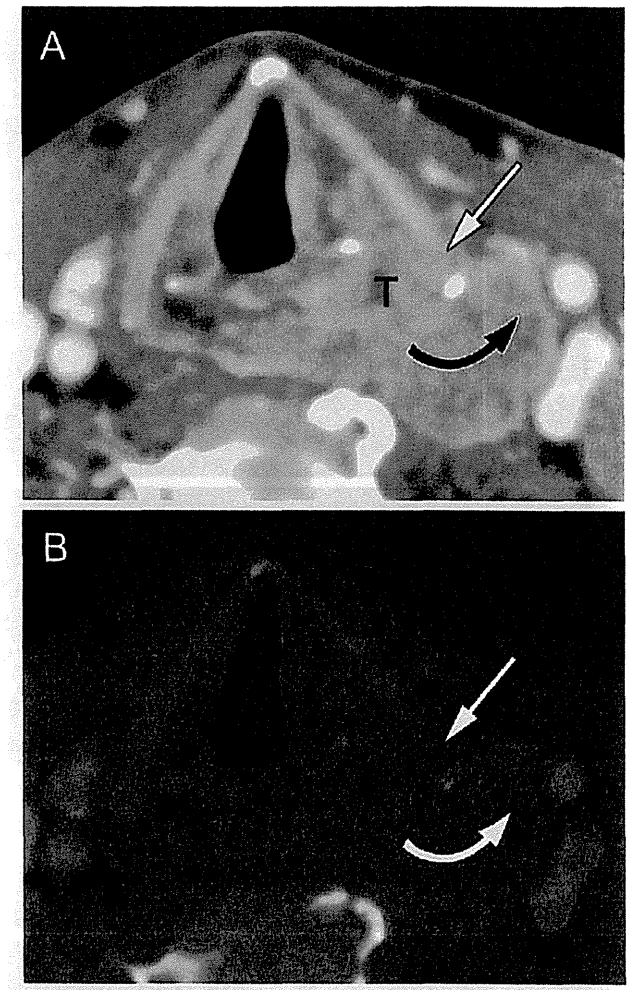

Fig. 13. Extralaryngeal spread via the inferior pharyngeal constrictor muscle on dual-energy CT in a 60-year-old man with hypopharyngeal cancer. WA image (A) and IO image (B) at the glottic level show a tumor mass (T) arising from the left piriform sinus, spreading into the lateral extralaryngeal soft tissue via the attachment of the inferior pharyngeal constrictor muscle (curved arrow). The tumor also wraps around the posterior border of the thyroid cartilage. On the WA image (A), the inner cortex of the left thyroid cartilage shows focal lysis (arrow). However, the IO image (B) shows no corresponding enhancement in the region indicated in the WA image (arrow). This case was evaluated as T4a disease without cartilage invasion and treated by chemoradiotherapy.

of their clinical history and a physical examination including nasopharyngoscopy, followed by multimodality imaging. We believe that dual-energy CT has the potential to become the primary diagnostic tool for laryngeal and hypopharyngeal cancer, although further investigation of dual-energy CT in comparison with MR will be necessary. Dual-energy CT may be very helpful for staging, including the definition of T stage, particularly when distinguishing T4 from lower-stage lesions, and for detection of regional lymph nodes (N staging) and distant metastasis (M staging). If evaluations conducted using dual-energy CT alone are insufficient, contrast-enhanced MR imaging is useful for excluding cartilage invasion, and for evaluation of very advanced local disease such as tumor invasion to the prevertebral fascia or carotid artery.

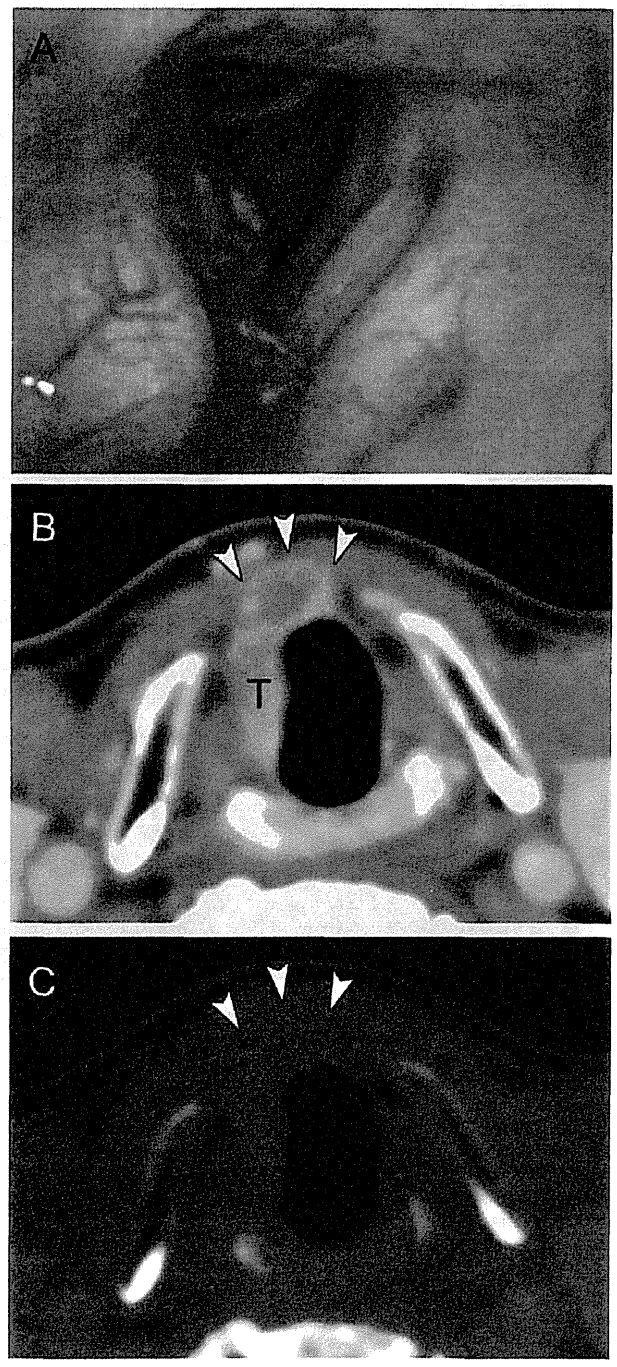

Fig. 14. Extralaryngeal spread via the cricothyroid membrane on dual-energy CT in a 72-year-old man with right glottic cancer. (A) Nasopharyngolaryngoscopy demonstrates the tumor mass (T) at the right glottis. It is diagnosed clinically as T3. WA image (B) and IO image (C) at the subglottic level show that the tumor has spread submucosally into the extralaryngeal soft tissue (arrowheads) via the cricothyroid membrane, and is therefore diagnosed as T4a.

6. Conclusion

Imaging plays a significant role in the staging of laryngeal and hypopharyngeal cancer, particularly when distinguishing the absence or presence of laryngeal cartilage invasion by the tumor and extralaryngeal spread. With conventional CT, although cartilage invasion can be diagnosed with acceptable accuracy by applying defined criteria for combinations of erosion, lysis and transmural extralaryngeal spread, iodine-enhanced tumors and non-ossified cartilage are sometimes difficult to distinguish. MR offers high contrast resolution for images without motion artifacts, although inflammatory changes in cartilage sometimes resemble cartilage invasion. With dual-energy CT, combined iodine-overlay images and weighted-average images can be used for evaluation of cartilage invasion, since iodine enhancement is evident in tumor tissue but not in cartilage. Extralaryngeal spread can be evaluated from CT, MR or dual-energy CT images and the three common routes of tumor spread into the extralaryngeal soft tissue must be considered. The ability to obtain weighted-average images and iodine-overlay images gives dual-energy CT potential advantages over conventional CT for evaluation of laryngeal and hypopharyngeal cancer. The benefit of the dual-energy technique lies in the impact of its high-quality images on treatment decision-making. Further advances in dual-energy CT may lead to its more widespread use for imaging of laryngeal and hypopharyngeal cancer. To define the most appropriate treatment strategies, it is important to thoroughly understand the potential applications, limitations, and advantages of existing and evolving imaging technologies, including dual-energy CT.

Conflict of interest

One of the authors (K.O.) is an employee of Siemens Japan. Authors who are not employees of Siemens Japan monitored and had control of inclusion of any data and information submitted for publication. No potential conflicts of interest were disclosed.

Acknowledgement

This work was supported in part by a National Cancer Center Research and Development Fund (23-A-35).

References

[1] Barnes L, Eveson JW, Riechart P, et al. Sedrs pathology and genetics of head and neck tumours. World Health Organization Classification of Tumours. Lyon: IARC; 2005. p. 107–62.
[2] Pfister DG, Laurie SA, Weinstein GS, et al. American Society of Clinical Oncology clinical practice guideline for the use of larynx-preservation strategies in the treatment of laryngeal cancer. J Clin Oncol 2006;24(22):3693–704.
[3] Hoffman HT, Porter K, Karnell LH, et al. Laryngeal cancer in the United States: changes in demographics, patterns of care, and survival. Laryngoscope 2006;116(9 Pt 2 Suppl 111):1–13.
[4] Forastiere AA, Goepfert H, Maor M, et al. Concurrent chemotherapy and radiotherapy for organ preservation in advanced laryngeal cancer. N Engl J Med 2003;349(22):2091–8.
[5] Knab BR, Salama JK, Solanki A, et al. Functional organ preservation with definitive chemoradiotherapy for T4 laryngeal squamous cell carcinoma. Ann Oncol 2008;19(9):1650–4.
[6] Worden FP, Moyer J, Lee JS, et al. Chemoselection as a strategy for organ preservation in patients with T4 laryngeal squamous cell carcinoma with cartilage invasion. Laryngoscope 2009;119(8):1510–7.
[7] Castelijns JA, Becker M, Hermans R. Impact of cartilage invasion on treatment and prognosis of laryngeal cancer. Eur Radiol 1996;6(2):156–69.
[8] Hermans R. Staging of laryngeal and hypopharyngeal cancer: value of imaging studies. Eur Radiol 2006;16(11):2386–400.
[9] Li B, Bobinski M, Gandour-Edwards R, Farwell DG, Chen AM. Overstaging of cartilage invasion by multidetector CT scan for laryngeal cancer and its potential effect on the use of organ preservation with chemoradiation. Br J Radiol 2011;84(997):64–9.
[10] Hartl DM, Landry G, Hans S, Marandas P, Brasnu DF. Organ preservation surgery for laryngeal squamous cell carcinoma: low incidence of thyroid cartilage invasion. Laryngoscope 2010;120(6):1173–6.
[11] Graser A, Johnson TR, Hecht EM, et al. Dual-energy CT in patients suspected of having renal masses: can virtual nonenhanced images replace true nonenhanced images? Radiology 2009;252(2):433–40.
[12] Gupta R, Phan CM, Leidecker C, et al. Evaluation of dual-energy CT for differentiating intracerebral hemorrhage from iodinated contrast material staining. Radiology 2010;257(1):205–11.
[13] Johnson TR, Krauss B, Sedlmair M, et al. Material differentiation by dual energy CT: initial experience. Eur Radiol 2007;17(6):1510–7.
[14] Kang MJ, Park CM, Lee CH, Goo JM, Lee HJ. Dual-energy CT: clinical applications in various pulmonary diseases. Radiographics 2010;30(3):685–98.

[15] Leschka S, Stolzmann P, Baumuller S, et al. Performance of dual-energy CT with tin filter technology for the discrimination of renal cysts and enhancing masses. Acad Radiol 2010;17(4):526–34.
[16] Kuno H, Onaya H, Iwata R, et al. Evaluation of cartilage invasion by laryngeal and hypopharyngeal squamous cell carcinoma with dual-energy CT. Radiology 2012;265(2):488–96.
[17] Sulfaro S, Barzan L, Querin F, et al. T staging of the laryngohypopharyngeal carcinoma. A 7-year multidisciplinary experience. Arch Otolaryngol Head Neck Surg 1989;115(5):613–20.
[18] Zbaren P, Becker M, Lang H. Pretherapeutic staging of laryngeal carcinoma. Clinical findings, computed tomography, and magnetic resonance imaging compared with histopathology. Cancer 1996;77(7):1263–73.
[19] Becker M, Burkhardt K, Dulguerov P, Allal A. Imaging of the larynx and hypopharynx. Eur J Radiol 2008;66(3):460–79.
[20] Edge SB BD, Compton CC, et al. (edrs) AJCC Cancer Staging Handbook (ed 7), New York, NY, Springer2010.
[21] Mendenhall WM, Parsons JT, Mancuso AA, Pameijer FJ, Stringer SP, Cassisi NJ. Definitive radiotherapy for T3 squamous cell carcinoma of the glottic larynx. J Clin Oncol 1997;15(6):2394–402.
[22] Mendenhall WM, Werning JW, Hinerman RW, Amdur RJ, Villaret DB. Management of T1–T2 glottic carcinomas. Cancer 2004;100(9):1786–92.
[23] Murakami R, Nishimura R, Baba Y, et al. Prognostic factors of glottic carcinomas treated with radiation therapy: value of the adjacent sign on radiological examinations in the sixth edition of the UICC TNM staging system. Int J Radiat Oncol Biol Phys 2005;61(2):471–5.
[24] Baum U, Greess H, Lell M, Nomayr A, Lenz M. Imaging of head and neck tumors - methods: CT, spiral-CT, multislice-spiral-CT. Eur J Radiol 2000;33(3): 153–60.
[25] Lell MM, Greess H, Hothorn T, Janka R, Bautz WA, Baum U. Multiplanar functional imaging of the larynx and hypopharynx with multislice spiral CT. Eur Radiol 2004;14(12):2198–205.
[26] Becker M, Zbaren P, Delavelle J, et al. Neoplastic invasion of the laryngeal cartilage: reassessment of criteria for diagnosis at CT. Radiology 1997;203(2):521–32.
[27] Brown CL, Hartman RP, Dzyubak OP, et al. Dual-energy CT iodine overlay technique for characterization of renal masses as cyst or solid: a phantom feasibility study. Eur Radiol 2009;19(5):1289–95.
[28] Karlo C, Lauber A, Gotti RP, et al. Dual-energy CT with tin filter technology for the discrimination of renal lesion proxies containing blood, protein, and contrast-agent. An experimental phantom study Eur Radiol 2011;21(2):385–92.
[29] Alvarez RE, Macovski A. Energy-selective reconstructions in X-ray computerized tomography. Phys Med Biol 1976;21(5):733–44.
[30] Hounsfield GN. Computerized transverse axial scanning (tomography). 1. Description of system. Br J Radiol 1973;46(552):1016–22.
[31] Kalender WA, Perman WH, Vetter JR, Klotz E. Evaluation of a prototype dual-energy computed tomographic apparatus.1. Phantom studies. Med Phys 1986;13(3):334–9.
[32] Kaza RK, Platt JF, Cohan RH, Caoili EM, Al-Hawary MM, Wasnik A. Dual-energy CT with single- and dual-source scanners: current applications in evaluating the genitourinary tract. Radiographics 2012;32(2):353–69.
[33] Krauss B, Schmidt B, Flohr T. Dual source CT. In: Johnson TRC, Fink C, Schönberg SO, Reiser MF, editors. Dual energy CT in clinical practice. 1st ed. Heidelberg, Dordrecht, London, New York: Springer; 2011. p. 11–20.
[34] Flohr TG, McCollough CH, Bruder H, et al. First performance evaluation of a dual-source CT (DSCT) system. Eur Radiol 2006;16(2):256–68.
[35] Tawfik AM, Kerl JM, Razek AA, et al. Image quality and radiation dose of dual-energy CT of the head and neck compared with a standard 120-kVp acquisition. AJNR Am J Neuroradiol 2011;32(11):1994–9.
[36] Paul J, Bauer RW, Maentele W, Vogl TJ. Image fusion in dual energy computed tomography for detection of various anatomic structures—effect on contrast enhancement, contrast-to-noise ratio, signal-to-noise ratio and image quality. Eur J Radiol 2011.
[37] Becker M. Neoplastic invasion of laryngeal cartilage: radiologic diagnosis and therapeutic implications. Eur J Radiol 2000;33(3):216–29.
[38] Becker M, Zbaren P, Laeng H, Stoupis C, Porcellini B, Vock P. Neoplastic invasion of the laryngeal cartilage: comparison of MR imaging and CT with histopathologic correlation. Radiology 1995;194(3):661–9.
[39] Beitler JJ, Muller S, Grist WJ, et al. Prognostic accuracy of computed tomography findings for patients with laryngeal cancer undergoing laryngectomy. J Clin Oncol 2010;28(14):2318–22.
[40] Nix PA, Salvage D. Neoplastic invasion of laryngeal cartilage: the significance of cartilage sclerosis on computed tomography images. Clin Otolaryngol Allied Sci 2004;29(4):372–5.
[41] Schmalfuss IM, Mancuso AA, Tart RP. Arytenoid cartilage sclerosis: normal variations and clinical significance. AJNR Am J Neuroradiol 1998;19(4):719–22.
[42] Munoz A, Ramos A, Ferrando J, et al. Laryngeal carcinoma: sclerotic appearance of the cricoid and arytenoid cartilage—CT-pathologic correlation. Radiology 1993;189(2):433–7.
[43] Gilbert K, Dalley RW, Maronian N, Anzai Y. Staging of laryngeal cancer using 64-channel multidetector row CT: comparison of standard neck CT with dedicated breath-maneuver laryngeal CT. Am J Neuroradiol 2010;31(2):251–6.
[44] Castelijns JA, Gerritsen GJ, Kaiser MC, et al. Invasion of laryngeal cartilage by cancer: comparison of CT and MR imaging. Radiology 1988;167(1):199–206.
[45] Becker M, Zbaren P, Casselman JW, Kohler R, Dulguerov P, Becker CD. Neoplastic invasion of laryngeal cartilage: reassessment of criteria for diagnosis at MR imaging. Radiology 2008;249(2):551–9.
[46] Hermans R, VanderGoten A, Baert AL. Image interpretation in CT of laryngeal carcinoma: a study on intra- and interobserver reproducibility. Eur Radiol 1997;7(7):1086–90.
[47] Hoorweg JJ, Kruijt RH, Heijboer RJJ, Eijkemans MJC, Kerrebijn JDF. Reliability of interpretation of CT examination of the larynx in patients with glottic laryngeal carcinoma. Otolaryngol Head Neck Surg 2006;135(1):129–34.
[48] Mancuso AA. Hypopharynx: malignant tumors. In: Mancuso AA, Hanafee WN, editors. Head and neck radiology. Philadelphia: Lippincott Williams & Wilkins; 2010. p. 2147–72.
[49] Mancuso AA. Larynx: malignant tumors. In: Mancuso AA, Hanafee WN, editors. Head and neck radiology. Philadelphia: Lippincott Williams & Wilkins; 2010. p. 1975–2022.
[50] Zbaren P, Egger C. Growth patterns of piriform sinus carcinomas. Laryngoscope 1997;107(4):511–8.

FULL PAPER

BJC

British Journal of Cancer (2014), 1–7 | doi: 10.1038/bjc.2014.49

Keywords: gemcitabine; iRGD peptide; neuropilin-1; pancreatic cancer; tumour graft

Anticancer effects of gemcitabine are enhanced by co-administered iRGD peptide in murine pancreatic cancer models that overexpressed neuropilin-1

Y Akashi[1], T Oda*[,1], Y Ohara[1], R Miyamoto[1], T Kurokawa[1], S Hashimoto[1], T Enomoto[1], K Yamada[1], M Satake[2] and N Ohkohchi[1]

[1]*Department of Surgery, Clinical Sciences, Graduate School of Comprehensive Human Sciences, University of Tsukuba, 1-1-1 Tennoudai, Tsukuba, 305-8575 Ibaraki, Japan and* [2]*Department of Diagnostic Radiology, Research Center for Innovative Oncology, National Cancer Center Hospital East, Kashiwa, Chiba, Japan*

Background: Impaired drug transport is an important factor that reduces the efficacy of anticancer agents against pancreatic cancer. Here, we report a novel combination chemotherapy using gemcitabine (GEM) and internalised-RGD (iRGD) peptide, which enhances tumour-specific drug penetration by binding neuropilin-1 (NRP1) receptor.

Methods: A total of five pancreatic cancer murine models (two cell line-based xenografts (CXs) and three tumour grafts (TGs)) were treated with either GEM (100 mg kg^{-1}, q3d × 4) alone or GEM plus iRGD peptide (8 μmol kg^{-1}). Evaluation of NRP1 expression in xenografts and 48 clinical cancer specimens was performed by immunohistochemistry (IHC).

Results: We identified a subset of pancreatic cancer models that showed NRP1 overexpression sensitive to iRGD co-administration. Treatment with GEM plus iRGD peptide resulted in a significant tumour reduction compared with GEM monotherapy in CXs, but not remarkable in TGs. Potential targets of iRGD were characterised as cases showing NRP1 overexpression (IHC-2+/3+), and these accounted for 45.8% of the clinical specimens.

Conclusions: Internalised RGD peptide enhances the effects of co-administered drugs in pancreatic cancer models, its efficacy is however only appreciable in those employing cell lines. Therefore, the clinical application needs to be given careful consideration.

Pancreatic cancer is one of the most intractable human malignancies, and the median survival of patients receiving the current standard therapeutic regimen with gemcitabine (GEM) is <6 months (Burris *et al*, 1997; Tempero *et al*, 2003). Insufficient therapeutic efficacy of anticancer drugs for solid tumours may be explained by the limited penetration of drugs into the cancer tissue (Ruoslahti *et al*, 2010). In fact, intravenously injected drugs are known to penetrate only a few cell diameters from blood vessels into the extravascular tumour tissue (Jain, 1999; Heldin *et al*, 2004). Therefore, a strategy for inducing drug hyperpermeability from tumour vessels might improve drug delivery to solid tumours.

Recently, a peptide known as iRGD (internalised-RGD) has developed (Sugahara *et al*, 2009, 2010). This peptide induces tumour-specific vascular hyperpermeability by binding to αv integrins that are specifically expressed on the endothelium of the tumour or angiogenic vessels. Co-administration of this peptide has been shown to markedly enhance the intratumoral accumulation of various agents with a wide range of molecular sizes in comparison with single administration, including doxorubicin (580 Da, 7-fold), dextran (1300–10 000 Da, 3- to 5-fold), Evans blue dye (66 000 Da, 2- to 4-fold), trastuzumab (148 000 Da, 40-fold), doxorubicin-liposome (Doxil, Janssen Pharmaceutica,

*Correspondence: Professor T Oda; E-mail: tatoda@md.tsukuba.ac.jp

Revised 27 December 2013; accepted 14 January 2014

Beerse, Belgium) (120 nm, 14-fold), and nab-paclitaxel (abraxane; Abraxis BioScience, Los Angeles, CA, USA) (130 nm, 9- to 12-fold), in mouse breast or prostate cancer models (Sugahara *et al*, 2010).

Activation of circulating iRGD peptide requires interaction with neuropilin-1 (NRP1) (Sugahara *et al*, 2009). Intravenously administered iRGD peptide initially accumulates in tumour vessels by binding to endothelial αv integrin, and then its C-terminus is cleaved to expose an arginine or lysine residue (= C-end rule (CendR) motif), before drug penetration deeply into the parenchyma of solid tumours occurs through interaction with NRP1 (Sugahara *et al*, 2009; Teesalu *et al*, 2009). Neuropilin-1 is a multifunctional non-tyrosine kinase receptor that binds to class 3 semaphorins and the vascular endothelial growth factor (VEGF) family, playing essential roles in mediating axonal guidance and angiogenesis (Soker *et al*, 1996; Kolodkin *et al*, 1997). It is reportedly correlated with tumour progression and/or poor prognosis in various cancers, including pancreatic cancer (Parikh *et al*, 2003; Hansel *et al*, 2004; Li *et al*, 2004; Fukahi *et al*, 2004; Müller *et al*, 2007). However, as the clinical sample sizes evaluated were limited, that is, only 10 cases or less, the expression profile and prognostic significance of NRP1 in pancreatic cancer has remained unclear.

The characteristics of iRGD peptide in solid cancers seem to warrant further investigation, especially in those with a dismal prognosis such as pancreatic cancer. However, there have been no comprehensive *in vivo* studies using pancreatic cancer models, and the effects of iRGD peptide used in combination with GEM, a key drug employed worldwide for treatment of pancreatic cancer, have not been tested. In the present study, therefore, we examined the effectiveness of iRGD peptide for boosting drug accumulation in eight different mouse pancreatic cancer xenograft models. The anticancer booster effect of combination therapy with GEM plus iRGD peptide was evaluated with reference to *in vivo* experiments and analysis of NRP1 expression in clinical cases of pancreatic cancer.

MATERIALS AND METHODS

Drugs. The iRGD peptide (Sequence; CRGDKGPDC, disulphide bridge; C1–C9, Purity; > 95%) we used for this study was delivered from a contract manufacturing company (American Peptide Company, Sunnyvale, CA, USA). A small quantity of the original iRGD peptide and control peptide (iRGE; CRGEKGPDC) were kindly provided by Drs Sugahara and Ruoslahti (UCSB, University of California, Santa Barbara), and the pharmaceutical power of our peptide was confirmed to be equivalent (data not shown). The other drugs purchased were Evans blue dye (MP Biomedicals, Santa Ana, CA, USA), dextran Alexa fluor 488 (D-22910, 10 000 Da MW; Molecular Probes, Eugene, OR, USA), and GEM (Gemzar; Eli Lilly, Indianapolis, IN, USA).

Cell lines and cell line-based models (= cell xenografts). The human pancreatic cancer cell lines AsPC-1 (CRL-1682), BxPC-3 (CRL-1687), and Capan-1 (HTB-79) were purchased from ATCC (Manassas, VA, USA). MIA PaCa-2 (JCRB0070) and SUIT-2 (JCRB1094) were purchased from JCRB Cell Bank (Osaka, Japan). AsPC-1, BxPC-3, and Capan-1 were cultured in RPMI-1640 medium (Sigma-Aldrich, MO, USA) with 10% fetal bovine serum. SUIT-2 and MIA PaCa-2 were cultured in Dulbecco's Modified Eagle Medium (DMEM; Sigma-Aldrich) with 5% and 10% fetal bovine serum. CXs were created by injecting these human pancreatic cancer cells (5×10^6 cells) into the dorsal subcutaneous space of C.B-17/Icr-scid/scid mice (female, 6 to 8 weeks old, CLEA Japan, Tokyo, Japan).

Transplant models using surgically removed tumour fragments (= tumor grafts). Pancreatic tumour grafts (TGs) were established by transplantation of fresh surgically resected tissue fragments of human pancreatic cancer. Samples were obtained under sterile conditions, avoiding apparently necrotic tissue and areas of normal pancreatic parenchyma. The samples were cut into $2 \times 2 \times 2$ mm pieces, placed immediately in normal saline solution, and cooled on ice until implantation (usually within 30 min to 1 h). All human samples employed in the experiments were harvested after informed consent in documents, and the establishment and the experimental use of 'tumour grafts' were approved by laboratory animal resource centre at University of Tsukuba. More details about the methods and characteristics of TGs are described in our previous report (Akashi *et al*, 2013).

***In vivo* systemic permeability assay.** Tumour-bearing mice were injected intravenously with 100 μl of PBS containing either 1% Evans blue dye or 0.3 mg of dextran. Internalised-RGD peptide (100 μl, 12 μmol kg^{-1}) or PBS was also injected *via* the tail vein 10 min beforehand. After 30 min of circulation, the mice were perfused with PBS containing 1% BSA, and their organs were collected. For Evans blue quantification, the dye was extracted from whole tumour tissue collected from each mice in *N*, *N*-dimethyl formamide (Sigma-Aldrich) for 24 h at 37 °C and quantified by measuring the absorbance at 600 nm with a spectrophotometer and the measured results were normalised by the tumour weight (Sugahara *et al*, 2010). Harvest tissues after dextran administration group were immediately fixed with 4% paraformaldehyde for 24 h, frozen in optimum cutting temperature (OCT) solution, and stored at − 80 °C.

Immunofluorescence. Tissue specimens frozen in OCT solution were sectioned (5 μm thick), mounted on slides, and air dried for 30 min. The primary antibody was goat anti-mouse CD31 (AF3628; R&D Systems, Minneapolis, MN, USA), and the secondary antibody was anti-goat Alexa Fluor 546 (Life Technologies, Grand Island, NY, USA). The sections showing immunofluorescence were scanned with a microscope (BZ-9000; Keyence Japan, Osaka, Japan).

Quantification of dextran distribution. Dextran distribution was evaluated by arbitrary selected four hotspots per tumour. These hotspots were selected from the central area of the tumour including cancer cell nests, and avoiding the peritumoral stromal areas. The fluorescent area above a certain threshold in each 200 magnification field was calculated using the Image J software (v1.44p, Rasvand, National Institutes of Health, USA), and the measurement results were averaged.

Tumour treatment study. Mice bearing tumours (two CXs (BxPC-3 and MIA PaCa-2) and three TGs (PC-03, 09, and 10)) received an intra-peritoneal injection of GEM (100 mg kg^{-1}) or saline (100 μl) twice a week for 2 weeks. The treatment was combined with intravenous injection of iRGD peptide at 8 μmol kg^{-1} or PBS 10 min before GEM injection. The mice were weighed and tumour volume was measured twice per week. All xenografts were harvested 28 days after the start of treatment. Tumour volume was calculated using the formula: volume (mm^3) = $(d^2 \times D)/2$, where d is the smallest and D is the largest tumour diameter.

Clinical specimens of pancreatic cancer. Forty-eight consecutive patients, who underwent surgery for pancreatic cancer at Tsukuba University Hospital between September 2003 and April 2009, were included in the study. Histologically proven cases of pancreatic ductal adenocarcinoma were included, and cancers derived from intraductal papillary mucinous neoplasms were excluded. None of the patients had received neo-adjuvant chemotherapy or irradiation before surgery. Specimens of pancreatic cancer tissue obtained with the patient's consent were fixed in 10% formalin solution and embedded in paraffin. The pathological diagnoses and classifications were made on the basis of the UICC TNM classification of malignant tumours, 7th edition (Sobin *et al*, 2009).

Immunohistochemistry. Paraffin-embedded sections were deparaffinised in xylene and dehydrated through a graded ethanol series. The sections were heated in Tris-EDTA buffer (pH 9.0) for 10 min at 121 °C in an autoclave for antigen retrieval, and endogenous peroxidase was quenched in 0.03% hydrogen peroxidase for 15 min. The specimens were then incubated with the primary antibody: anti-NRP1 (sc-5307, 1 : 50; Santa Cruz Biotechnology, Santa Cruz, CA, USA) overnight at 4 °C, or anti-CD31 (LS-B1932; LifeSpan BioSciences, Seattle, WA, USA) for 1 h at room temperature. The remaining steps were carried out with the Envision + System-HRP (DAKO, Glostrup, Denmark), followed by counterstaining with haematoxylin. Specificity of this antibody was verified by immunostaining of human kidney tissue samples. To assess tissue NRP1 expression, the sections were scored semi-quantitatively (on a scale of Immunohistochemistry (IHC)-0–3: negative = 0, weak = 1, moderate = 2, and strong = 3) according to the intensity of chromogen deposition in 10% or more of the neoplastic cells.

Microvessel density. Microvessel density (MVD) was measured by counting the number of CD31-positive blood vessels at selected

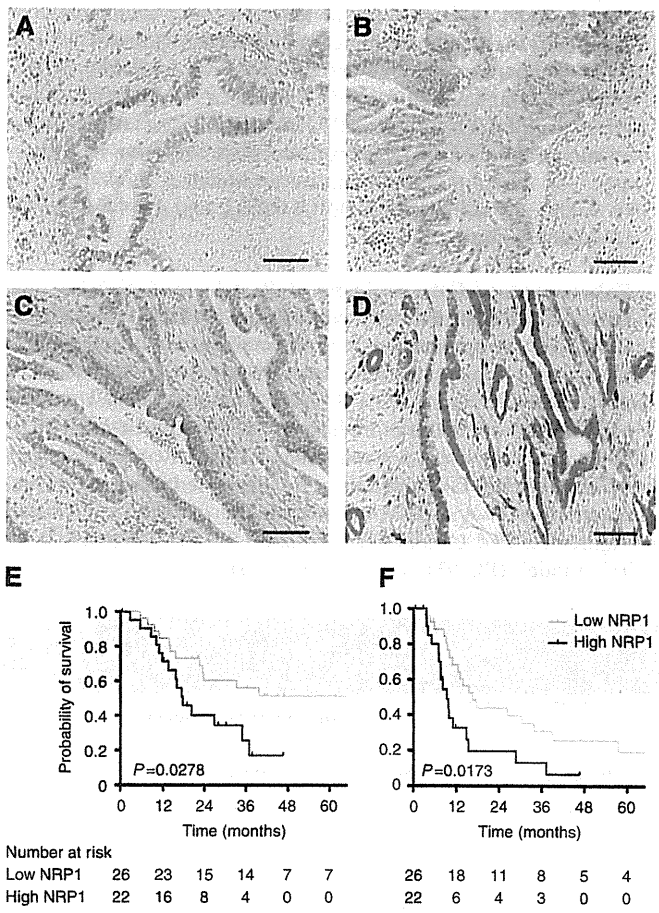

Figure 1. **(A–D)** Representative photomicrographs showing immunohistochemical staining and detailed expression of neuropilin-1 (NRP1, brown colour) in pancreatic ductal adenocarcinomas. Nine (18.8%) cases were negative (IHC-0, **A**), 17 (35.4%) were weakly positive (IHC-1 +, **B**), 12 (25.0%) were moderately positive (IHC-2 +, **C**), and 10 (20.8%) were strongly positive (IHC-3 +, **D**). (**E** and **F**) Kaplan–Meier analysis of overall survival (**E**) and disease-free survival (**F**) in relation to low (IHC-0/1 +) or high (IHC-2 + /3 +) NRP1 expression in pancreatic cancer. Patients with high NRP1 expression showed shorter overall survival ($P = 0.0278$) and disease-free survival ($P = 0.0173$) than patients with low NRP1 expression.

Table 1. Correlation between neuropilin-1 (NRP1) expression and clinicopathological parameters of patients with pancreatic cancer

		NRP1 level			
Characteristics	**All cases**	**Low**	**High**	χ^2	***P*-value**
Total participants	48	26	22		
Age at surgery (years)					
<60	14	8	6	0.003	0.958
⩾60	34	18	16		
Gender					
Male	24	13	11	0.084	0.772
Female	24	13	11		
Tumour grade					
Well	2	1	1	0.031	0.985
Moderately	44	24	20		
Poorly	2	1	1		
Tumour location					
Head	40	23	17	0.420	0.517
Body/Tail	8	3	5		
Tumour size					
<40 mm	29	16	13	0.015	0.902
⩾40 mm	19	10	9		
T factor					
T1/T2	2	2	0	1.812	0.404
T3	16	8	8		
T4	30	16	14		
Lymph-node metastasis					
Positive	35	17	18	0.904	0.342
Negative	13	9	4		
Vascular invasion					
Positive	12	4	8	1.790	0.181
Negative	36	22	14		
Perineural invasion					
Positive	24	11	13	0.755	0.385
Negative	24	15	9		
Microvessel density[a]					
<25	16	13	3	5.549	0.018
⩾25	32	13	19		
Resection margin					
Positive	13	7	6	0.089	0.765
Negative	35	19	16		
CEA					
Normal	20	13	7	0.959	0.327
High	28	13	15		
CA19-9					
Normal	16	12	4	3.032	0.082
High	32	14	18		

Abbreviation: CEA=carcinoembryonic antigen.
[a]Number of vessels per 100 magnification field.